Electrochimica Acta 253 (2017) 85–92

Contents lists available at ScienceDirect

Electrochimica Acta

journal homepage: www.elsevier.com/locate/electacta

Investigation of cycling-induced microstructural degradation in silicon-based electrodes in lithium-ion batteries using X-ray nanotomography

Oluwadamilola O. Taiwo[a], Melanie Loveridge[b], Shane D. Beattie[c], Donal P. Finegan[a], Rohit Bhagat[b], Daniel J.L. Brett[a], Paul R. Shearing[a,*]

[a] Electrochemical Innovation Lab, Department of Chemical Engineering, University College London, WC1E 7JE, UK
[b] WMG, University of Warwick, Coventry, CV4 7AL, UK
[c] BTInnovations, 32 Bobbit Drive, St. Croix, Nova Scotia, B0N 2E0, Canada

ARTICLE INFO

Article history:
Received 9 June 2017
Received in revised form 15 August 2017
Accepted 27 August 2017
Available online 31 August 2017

Keywords:
3D imaging
Silicon electrode
Lithium-Ion battery cycling
X-ray nano-CT
Battery degradation

ABSTRACT

The microstructural degradation of a composite silicon electrode at different stages in its cycle life was investigated in 3D using X-ray nano-computed tomography. A reconstructed volume of 36 μm × 27 μm × 26 μm from the composite electrode was imaged in its pristine state and after 1, 10 and 100 cycles. Particle fracturing and phase transformation was observed within the electrode with increased cycling. In addition, a distinct, lower X-ray attenuating phase was clearly resolved, which can be associated with surface film formation resulting from electrolyte breakdown and with silicon particle phase transformation. Changes in quantified microstructural properties such as phase volume fraction and particle specific surface area were tracked. Electrode performance loss is associated with loss of active silicon. These imaging results further highlight the capability of high resolution X-ray tomography to investigate the role of electrode microstructure in battery degradation and failure.

1. Introduction

The increasing demand for more energy-dense lithium-ion batteries (LIBs), particularly in large scale applications such as grid-scale energy storage and electric vehicles, has led to the exploration of the use of alternative electrode materials. With a theoretical specific capacity ten times higher than that of conventional graphite electrodes – 3579 mAh/g –, silicon (Si) is a promising electrode material [1]. However, silicon suffers rapid capacity fade and short cycle life mainly as a result of the significant volume changes (up to 280% [1]) that it experiences upon lithiation, causing cracking and pulverisation within the electrode, which leads to loss of electrical contacts [2,3].

In an attempt to improve the performance and lifetime of silicon electrodes, significant research effort has been devoted towards the use of nanostructured silicon materials [4–8]. However, issues such as significant solid electrolyte interphase (SEI) formation, as well as the difficulty and high cost of manufacturing scale-up prevent their application in commercial lithium ion batteries [8,9]. These drawbacks show micron-sized silicon particles to still be a favourable option as electrode materials, since they are low-cost, commercially available and can be used to create electrodes with higher volumetric energy density compared with nano-sized silicon-alloy particles.

To overcome this challenge of designing a commercially-viable silicon electrode, an improved understanding of the influence of silicon microstructure on battery performance is required. X-ray computed tomography (CT) is a powerful, non-invasive diagnostic tool that has been used to elucidate the three-dimensional microstructure of a wide variety of materials, including lithium-ion battery electrodes [10–15], and the rapid proliferation of X-ray imaging techniques over the past decade has enabled characterisation of material microstructures with unprecedented resolution at multiple length and time scales using both laboratory and synchrotron sources [16–20].

Recently, X-ray CT has been used to study the lithiation-induced evolution of Si electrodes, and has enabled investigation of electrode delamination [21], bulk electrode volume expansion and phase changes [22,23], and particle cracking and pulverisation [24–27]. However, these 3D X-ray imaging studies on silicon electrodes were performed at the early stages of electrode cycle life (first half cycle or first full cycle), with spatial resolutions down to

* Corresponding author.
E-mail address: p.shearing@ucl.ac.uk (P.R. Shearing).

http://dx.doi.org/10.1016/j.electacta.2017.08.161

ca. 2 μm being achieved [23,27]. Recent advances in laboratory X-ray tomography have enabled even higher spatial resolutions to be achieved, down to 50 nm [17]. Here for the first time, we study the 3D morphological transformation of a Si electrode over several charge-discharge cycles using high resolution laboratory X-ray nano-CT at a spatial resolution of 150 nm.

2. Experimental

2.1. Electrode preparation and cell fabrication

Powdered Si (Elkem Silgrain e-Si, d_{50} 3.1 μm, 99.7% purity) was used as active material. Carbon black (Alfa Aesar, Acetylene Black, purity, 99.9+ %) and graphite (TIMREX SF56, purity 99.93%) were used as conductive agents and a sodium salt of polyacrylic acid (Na-PAA) as binder. The binder was prepared by dissolving PAA in de-ionised water and then partially neutralizing the solution with sodium carbonate; details of the binder preparation can be found in [28].

The powdered Si, carbon additives and the partially neutralized Na-PAA solution (in a percentage weight ratio of 70:16:14, respectively) were mixed with de-ionised water, and stirred using a high shear mixer (Primix Homodisper Model 2.5) for 30 mins. Electrode laminates were then created by casting the resulting electrode slurry onto 10 μm thick Cu foil (Oak Mitsui, electro-deposited) using a film applicator (RK PrintCoat Instruments, UK), with partial vacuum applied to the Cu foil and a doctor blade gap set to 100 μm. Slurry-coated Cu foils were dried on a hot plate at 80 °C for 2 mins followed by vacuum drying (7 mbar) at 70 °C for 12 h. The dried electrode laminates were cut into 10 mm diameter discs, each of which was weighed in order to obtain the mass loading of Si.

Half-cells were fabricated using PFA-type Swagelok hardware (PFA-820-6, 0.5 inch diameter, Swagelok, USA) in an argon-filled glove-box (oxygen and moisture levels in the glove-box were both maintained at <0.5 ppm) with a metallic lithium foil counter electrode (Pi-KEM Ltd, cut to 11 mm diameter), a borosilicate glass fibre separator (Whatmann GF-D grade, GE, cut to 12 mm diameter), and electrolyte containing 1 M $LiPF_6$ in mixture of ethylene carbonate (EC): ethyl methyl carbonate (EMC) in the ratio 3:7 by volume.

2.2. Electrochemical characterisation

Electrochemical cycling of assembled Swagelok cells was performed between 1–0.005 V (vs. Li/Li^+) at room temperature using a Maccor 4300 series battery cycler. Cells were selected to be cycled for 1, 10 and 100 cycles. A C/5 rate was used for Si electrodes cycled for 1 and 10 cycles. For electrodes cycled for 100 cycles, the first cycle was performed at a C/5 rate to promote SEI formation, and subsequent cycles were performed at a C/2 rate. The C-rates were calculated based on the theoretical capacity of Si at room temperature ($Q = 3579\ mAhg^{-1}$).

After charge cycling, electrochemical impedance spectroscopy (EIS) measurements were performed on each cell using an Ivium CompactStat.e electrochemical workstation (Ivium Technologies, Netherlands). Impedance spectra were acquired with the Si electrodes in the de-lithiated state after 1, 10 and 100 cycles over a frequency range of 100 kHz to 1 mHz, with an AC signal amplitude of 5 mV.

2.3. Scanning electron microscopy (SEM) and X-ray nanotomography

After electrochemical testing, the cycled cells were then carefully disassembled in an argon-filled glove box. The Si electrodes (in de-lithiated state) were carefully extracted from the disassembled cells and then thoroughly rinsed in pure diethyl carbonate (DEC) solution for 6 h to remove traces of electrolyte. The washed electrode was dried by storing it in the evacuated antechamber of the glove box at room temperature to remove any DEC present.

Both the pristine (uncycled) and the washed, cycled versions of the Si electrode sample were then dissected under a visible light microscope (into smaller sample sizes suitable for nanoscale X-ray CT imaging (<500 μm length) and mounted onto the tip of stainless steel needles using epoxy resin. Remaining portions of the pristine and cycled electrodes were reserved for SEM characterisation. Scanning electron micrographs of electrode sample in its pristine and cycled states were captured with the aid of a ZEISS EVO MA 10 microscope.

The electrode samples were then imaged in a laboratory-based nano-scale X-ray microscope (ZEISS Xradia 810 Ultra, Carl Zeiss Microscopy, Pleasanton, CA) using an absorption contrast tomography setting [29]. For each investigated sample, X-ray radiographs were acquired over a 180° sample rotation; details of the tomographic imaging parameters for each sample are presented in Table 1. The acquired radiograph images were then reconstructed into a 3D volume using ZEISS XMReconstructor software (Carl Zeiss X-ray Microscopy Inc., Pleasanton) which employs a filtered-back projection algorithm [30].

2.4. 3D image analysis and quantification

Image processing and volume rendering of each of the reconstructed electrode datasets was carried out using the Avizo software package (v9.1, FEI VSG, France). From within each 3D electrode dataset, a volume of interest (36 μm × 27 μm × 26 μm) was extracted for further analysis. An anisotropic diffusion filter [31] was applied to the cropped 3D greyscale image datasets to minimize random image noise while preserving significant image features, after which a segmentation procedure combining thresholding and 3D region growing was implemented to distinguish between the solid and pore phases based on their greyscale intensity values.

3D quantification of the segmented datasets was also performed in Avizo software; phase volume fraction and volume-specific surface area values, which are important morphological parameters that determine electrode performance, were calculated. Phase volume fraction was calculated using a voxel counting approach as the ratio of the total number of voxels in a particular phase to the total number of voxels in the analysed volume. For surface area calculations, triangulated surface meshes were generated from the segmented image datasets using a marching cubes algorithm [32], and then subsequently smoothed using sub-voxel weights.

3. Results and Discussion

The discharge capacity and Coulombic efficiency profiles of the Si electrode over a 100 cycle period are shown in Fig. 1. At a C/5 rate, a discharge capacity of *ca.* 2700 $mAhg^{-1}$ was obtained in the first

Table 1
X-ray CT image acquisition parameters.

	Pristine	1st cycle	10th cycle	100th cycle
No. of radiographs recorded	1601	2001	2001	2001
Radiograph exposure time (s)	23	15	20	14
Effective voxel size (nm)	63.1			
Photon energy (keV)	5.4			
Field of view dimensions	65 μm × 65 μm			
Detector binning	1			

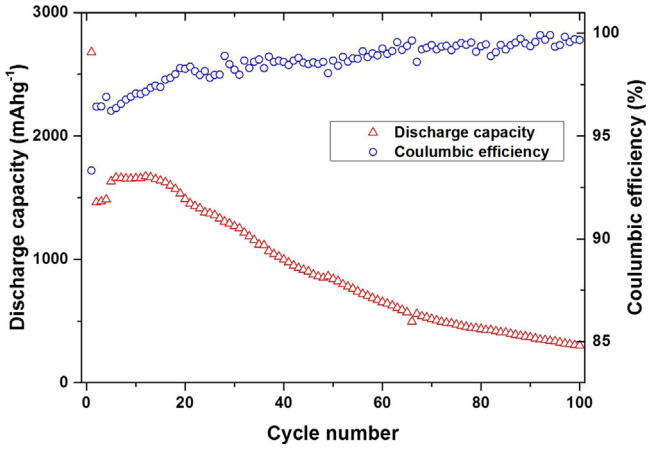

Fig. 1. Discharge capacity and Coulombic efficiency versus cycle number for the Si electrode.

cycle but this sharply drops to *ca.* 1460 mAhg^{-1} in the second cycle. This significant capacity loss after the first cycle can be attributed to the formation of SEI on the surface of the silicon electrode particles. The capacity slightly recovers to over 1600 mAhg^{-1} after the fifth cycle, and remains relatively stable until the 15th cycle after which a steady decline in electrode performance is seen with progressive cycling. The Coulombic efficiency (CE) was calculated as the percentage ratio of the electrode's de-lithiation capacity to its lithiation capacity. As the SEI layer on LIB electrodes matures and its growth slows down with cycling, the CE is expected to increase and then stabilize shortly after the first few cycles [33]. The CE of Si was 93.3% in the first cycle, and it is seen to increase and then stabilize above 98% after 20 cycles.

To gain further insight into the capacity fade occurring in the Si electrode, EIS measurements were performed on the cycled electrodes. The changes in impedance spectra of the Si electrode in the de-lithiated state after 1, 10 and 100 cycles are shown as Nyquist plots in Fig. 2a. The Nyquist plots were fitted by the equivalent circuit shown in Fig. 2b. The high-to-medium frequency semi-circles generally reflect Li^+ migration through multilayer surface films (represented by R_{SEI} and CPE_1 in the equivalent circuit model), the interphase electronic contacts between the conductive/binder matrix and the current collector (represented by R_{int} and CPE_2) and charge transfer resistance between the SEI layer and the electrode interface (represented by R_{ct} and CPE_3) [34–36]. The sloping linear curve in the low frequency region, referred to as the Warburg impedance (Z_w), corresponds to the solid state diffusion of lithium through the Li-Si alloy material [34,37]. The high-frequency intercept (R_s), which reflects the series resistance of current collectors, electrodes, electrolyte, and electrical connections [38], showed minimal change with cycling.

The high-to-medium frequency impedance spectra were enlarged in the inset of Fig. 2a for more clear observation. The magnitude of the high frequency semi-circle increased with cycle number, suggesting an increase in surface film resistance of the electrode and double-layer at the electrode-electrolyte interface. This surface film resistance change is also evident from the increase in R_{SEI} values in Fig. 2c, and could be attributed to the formation of a thicker SEI layer with progressive cycling. The R_{ct} value is seen to drop after the 10th cycle and then increase after 100 cycles. The lower R_{ct} after 10th cycle compared with the 1st cycle could be associated with the capacity drop and recovery between the 2nd and 7th cycles. Following the 1st discharge-charge cycle, the large volume change within the electrode may have caused a disconnection of electronic contact between the Si particles and the conductive additive/binder matrix leading to the

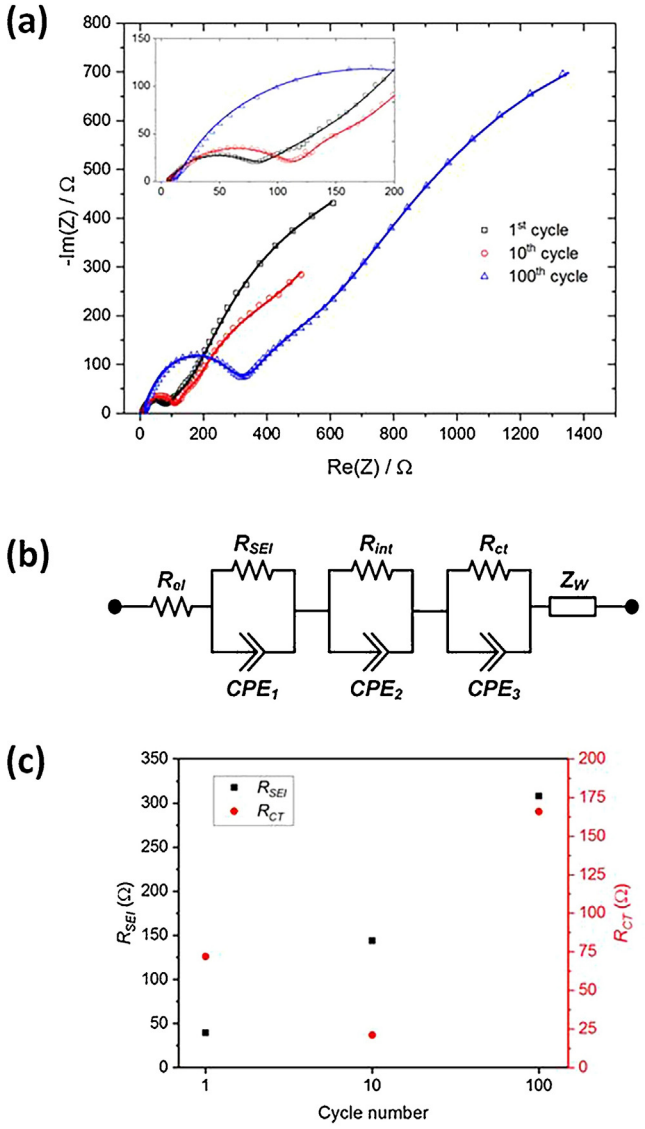

Fig. 2. (a) Nyquist plots of the Si electrode in de-lithiated state after different cycles. (b) Equivalent circuit used to model the impedance spectra in (a). (c) Surface film resistance and charge transfer resistance as a function of cycle number.

initial capacity drop in subsequent cycles. However, the repeated expansion and contraction within the electrode may have restored some electronic contact with the conductive matrix after the 7th cycle, causing the slight capacity loss.

Fig. 3a–d shows the surface view scanning electron micrographs of the morphology of the silicon electrode in its pristine state (before cycling) and after the 1st, 10th cycle, and 100th cycles. In Fig. 3a, the individual silicon particles can be easily identified by their sharp edges and flat faces. After 1 cycle (Fig. 3b), the electrode still maintains its microstructural integrity; however, the sharp edges and faces become less prominent as a result of the SEI layer formation and lithiation-induced volume changes. Surface film formation becomes significant after 10 cycles (Fig. 3c), along with the occurrence of cracks propagating across the electrode surface. The micrograph taken after 100 cycles (Fig. 3d) shows severe pulverisation of electrode particles into smaller fragments.

In order to gain further insight into the morphological evolution of the Si electrode, 3D nano-scale X-ray tomography was performed on the pristine and cycled electrodes. Fig. 4 shows 2D greyscale image cross-sections through the 3D X-ray

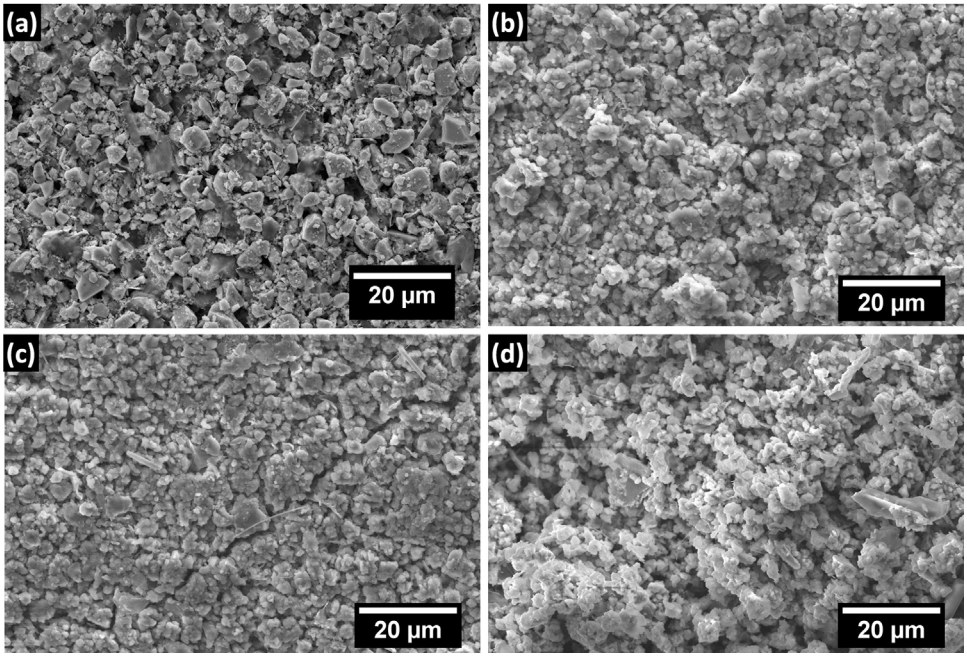

Fig. 3. SEM images of the silicon electrode (a) in its pristine state (b) after 1 cycle, (c) after 10 cycles, and (d) after 100 cycles.

tomograms of the Si electrode before cycling, after 1, 10 and 100 cycles. To facilitate the comparison between the different tomograms, the greyscale intensity histogram of each X-ray tomogram was normalized with respect to the initial tomogram of the pristine electrode. Within the pristine electrode (Fig. 4a), the Si particles are clearly distinguished by their higher X-ray attenuation as the bright, irregular-shaped regions with no visible cracks or fracturing. The darker, less attenuating region surrounding the Si particle corresponds to the porous matrix containing the conductive material and binder phases.

Following the 1st cycle, (Fig. 4b), significant fracturing and deformation can be seen to occur within the Si particles (denoted by yellow arrows in the reconstructed cross section and observed in the 3D particle rendering in Fig. 4b) as a result of volume change caused by lithiation and de-lithiation processes. In addition to particle fracturing, the Si particles begin to lose the (greyscale) intensity around their edges, with the presence of a relatively low intensity/low attenuation phase observed around the outer surface of the particles. This decrease in greyscale intensity directly correlates with a decrease in X-ray absorption or a change in material density [24]. The formation of the low attenuating phase can be attributed to the phase transformation that occurs due to the alloying of Li and Si, as well as the significant formation of SEI-based products from electrolyte breakdown. Excessive SEI formation in Si electrodes can be controlled through the use of electrolyte additives [35,39].

After 10 cycles (Fig. 4c) and 100 cycles (Fig. 4d), numerous Si particles appear to have undergone further phase transformation and fracturing, and this is accompanied by a significant increase in the low attenuating phase surrounding the remaining Si fragments. However, at 100 cycles, the region that was imaged within the electrode appeared to have lower attenuating, void-like regions (highlighted by blue arrows in Fig. 4d) which could be attributed to the bulk fracturing and material displacement within the electrode matrix as a result of repeated volume change during progressive cycling. This could influence the electrical contact of some Si particles within the bulk electrode, causing their isolation from the conductive matrix and could contribute to the loss in electrode capacity.

The evolution of the 3D structure of the Si electrode was also visualized with the aid of 3D renderings of the electrode. Fig. 5 shows a 3D rendering of the Si phase within the electrode prior to any electrochemical cycling. The crystalline Si particles (colored in yellow) were rendered after threshold segmentation of the highly attenuating Si particles shown in Fig. 4, while the rest of the electrode matrix (conductive carbon, binder and pore phases) were set to be invisible.

3D renderings of the electrode highlighting the Si and low attenuating phases after 1, 10 and 100 cycles are presented in Fig. 5b–d. 3D quantitative analysis of the electrode volumes showed a significant reduction in the volume fraction of the crystalline Si phase in the analysed electrode volume, from 21.30% in electrode's pristine state to 3.65% after 100 cycles (Table 2). The decreased in crystalline Si phase fraction with cycle number can be associated with particle pulverisation and irreversible phase changes from crystalline Si (c-Si) to amorphous lithium silicide (a-Li_xSi). The surface area-to-volume ratio of this Si phase is seen to increase between the analysed 3D volumes from 2.86 $\mu m^2/\mu m^3$ in the pristine electrode to 4.29 $\mu m^2/\mu m^3$ after 1st cycle; this change can be associated with the increased Si surface area exposed due to particle fracturing upon volume expansion. The surface area drops slightly in the examined electrode volume at 100 cycles to 3.45 $\mu m^2/\mu m^3$ most likely due to a lower volume fraction of Si particles or fragments present.

4. Conclusions

Upon cycling, Si electrodes experience significant degradation in their electrochemical performance which can be related to changes within the electrode microstructure. Here, for the first time, X-ray nano-computed tomography was used to investigate morphological evolution of the 3D microstructure of a Si-based electrode over several charge-discharge cycles. Fracturing and phase transformation of Si particles within the electrode material were highlighted, and the evolution of morphological parameters such as phase volume fraction and specific surface area as a result of the electrode cycling were quantified in 3D. Such high-resolution, nanometre-scale X-ray imaging, in combination

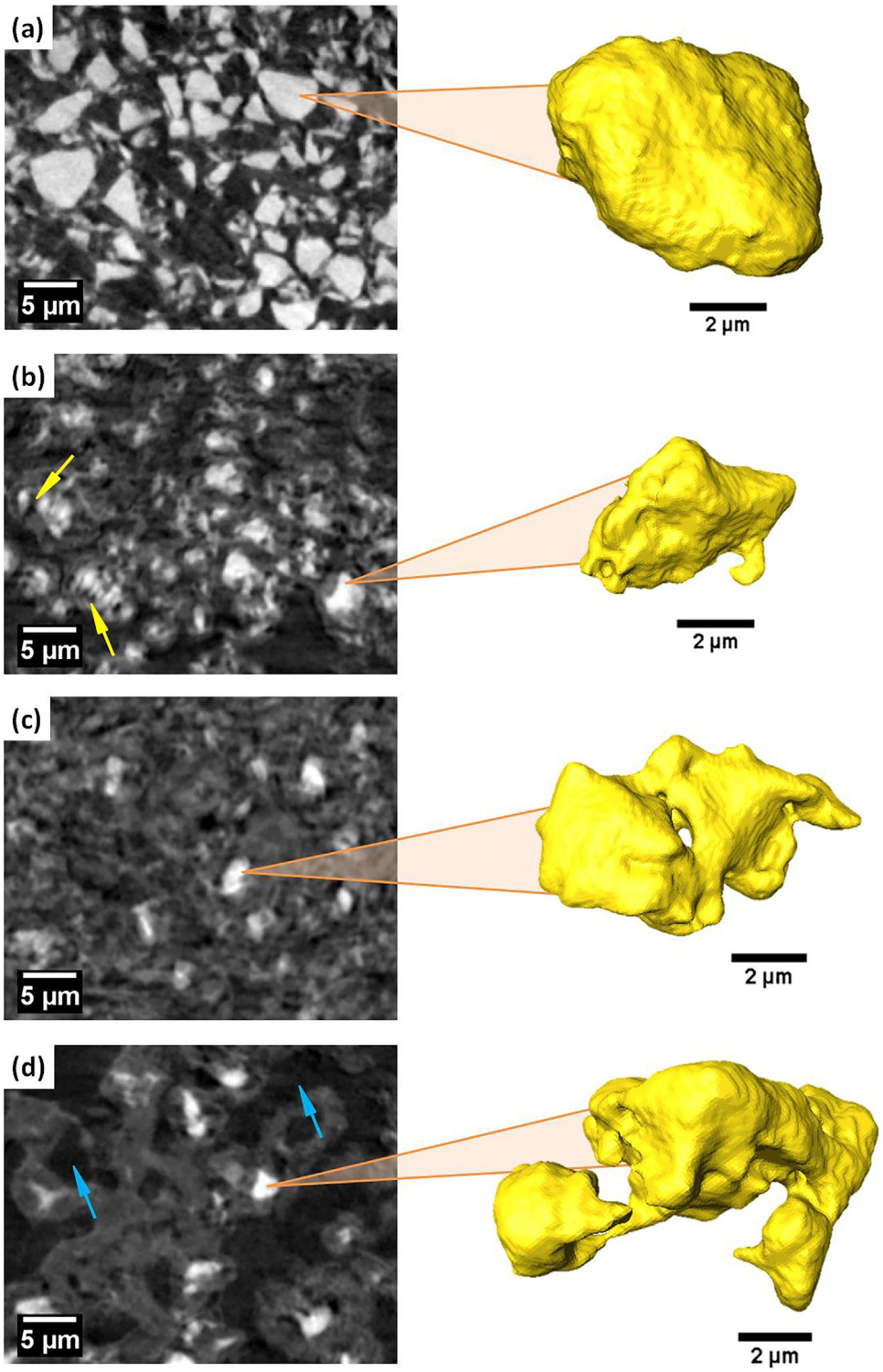

Fig. 4. Cross-sections through X-ray tomograms of the Si electrode (a) in its pristine state, (b) after 1 cycle, (c) after 10 cycles, and (d) after 100 cycles. 3D visualisation of crystalline Si particles after the different cycle stages is shown on the right-hand side. The yellow arrows in (b) highlight fracturing in the bulk Si particles while the blue arrows in (d) highlight what appear to be voids possibly formed from fracturing and material displacement due to repeated electrode volume changes.

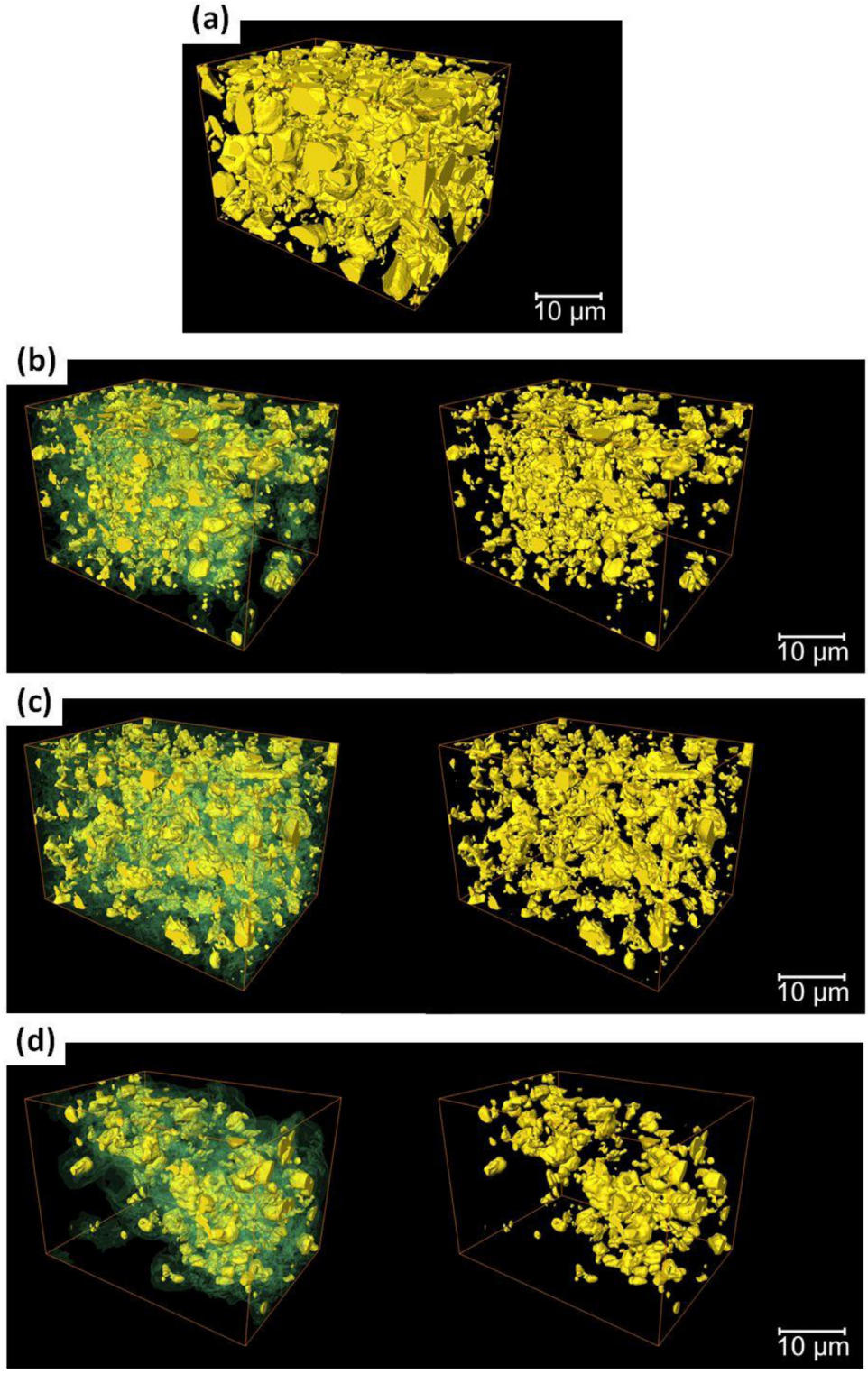

Fig. 5. (a) 3D rendering of the pristine Si electrode particles. (b–d) show 3D renderings of the electrode after 1, 10 and 100 cycles respectively. Left: 3D rendering showing both Si phase (yellow) and low attenuating phase (transparent green). Right: 3D rendering of Si phase only. (For interpretation of the references to color in this figure legend, the reader is referred to the web version of this article.)

Table 2
Morphological parameters extracted from the 3D reconstructions of the electrode before and after cycling.

Cycle number	Phase volume fraction (%)		Pure Si specific surface area ($\mu m^2/\mu m^3$)
	Pure Si phase	Low-attenuating phase	
0	21.30	–	2.86
1	5.84	44.10	4.29
10	5.48	79.92	4.36
100	3.65	46.01	3.45

with impedance measurements, provides opportunities to obtain better understanding of the electrochemically-induced degradation mechanisms in lithium-ion batteries.

Acknowledgements

The authors would like to thank the UK EPSRC for funding under grants EP/M009394/1, EP/N001583/1, and EP/N032888/1.

References

[1] M.N. Obrovac, L.J. Krause, Reversible Cycling of Crystalline Silicon Powder, J. Electrochem. Soc. 154 (2007) A103–A108, doi:http://dx.doi.org/10.1149/1.2402112.
[2] L.Y. Beaulieu, K.W. Eberman, R.L. Turner, L.J. Krause, J.R. Dahn, Colossal Reversible Volume Changes in Lithium Alloys, Electrochem. Solid-State Lett. 4 (2001) A137––A140, doi:http://dx.doi.org/10.1149/1.1388178.
[3] T.D. Hatchard, J.R. Dahn, In Situ XRD and Electrochemical Study of the Reaction of Lithium with Amorphous Silicon, J. Electrochem. Soc. 151 (2004) A838––A842, doi:http://dx.doi.org/10.1149/1.1739217.
[4] C.K. Chan, H. Peng, G. Liu, K. McIlwrath, X.F. Zhang, R.A. Huggins, Y. Cui, High-performance lithium battery anodes using silicon nanowires, Nat. Nanotechnol. 3 (2008) 31–35, doi:http://dx.doi.org/10.1038/nnano.2007.411.
[5] K. Peng, J. Jie, W. Zhang, S.-T. Lee, Silicon nanowires for rechargeable lithium-ion battery anodes, Appl. Phys. Lett. 93 (1–3) (2008) 033105, doi:http://dx.doi.org/10.1063/1.2929373.
[6] I. Kovalenko, B. Zdyrko, A. Magasinski, B. Hertzberg, Z. Milicev, R. Burtovyy, I. Luzinov, G. Yushin, A Major Constituent of Brown Algae for Use in High-Capacity Li-Ion Batteries, Science 80 (334) (2011) 75–79, doi:http://dx.doi.org/10.1126/science.1209150.
[7] G. Liu, S. Xun, N. Vukmirovic, X. Song, P. Olalde-Velasco, H. Zheng, V.S. Battaglia, L. Wang, W. Yang, Polymers with Tailored Electronic Structure for High Capacity Lithium Battery Electrodes, Adv. Mater. 23 (2011) 4679–4683, doi:http://dx.doi.org/10.1002/adma.201102421.
[8] H. Wu, Y. Cui, Designing nanostructured Si anodes for high energy lithium ion batteries, Nano Today. 7 (2012) 414–429, doi:http://dx.doi.org/10.1016/j.nantod.2012.08.004.
[9] A. Magasinski, P. Dixon, B. Hertzberg, A. Kvit, J. Ayala, G. Yushin, High-performance lithium-ion anodes using a hierarchical bottom-up approach, Nat. Mater. 9 (2010) 353–358, doi:http://dx.doi.org/10.1038/nmat2725.
[10] D.S. Eastwood, R.S. Bradley, F. Tariq, S.J. Cooper, O.O. Taiwo, J. Gelb, A. Merkle, D. J.L. Brett, N.P. Brandon, P.J. Withers, P.D. Lee, P.R. Shearing, The application of phase contrast X-ray techniques for imaging Li-ion battery electrodes, Nucl. Instruments Methods Phys. Res. Sect. B Beam Interact. with Mater. Atoms. 324 (2014) 118–123, doi:http://dx.doi.org/10.1016/j.nimb.2013.08.066.
[11] O.O. Taiwo, D.P. Finegan, D.S. Eastwood, J.L. Fife, L.D. Brown, J.A. Darr, P.D. Lee, D.J.L. Brett, P.R. Shearing, Comparison of three-dimensional analysis and stereological techniques for quantifying lithium-ion battery electrode microstructures, J. Microsc. (2016) 1–13, doi:http://dx.doi.org/10.1111/jmi.12389.
[12] D.P. Finegan, E. Tudisco, M. Scheel, J.B. Robinson, O.O. Taiwo, D.S. Eastwood, P. D. Lee, M. Di Michiel, B. Bay, S.A. Hall, G. Hinds, D.J.L. Brett, P.R. Shearing, Quantifying Bulk Electrode Strain and Material Displacement within Lithium Batteries via High-Speed Operando Tomography and Digital Volume Correlation, Adv. Sci. 3 (1–11) (2015) 1500332, doi:http://dx.doi.org/10.1002/advs.201500332.
[13] M. Ebner, F. Marone, M. Stampanoni, V. Wood, Visualization and quantification of electrochemical and mechanical degradation in Li ion batteries, Science. 342 (2013) 716–720, doi:http://dx.doi.org/10.1126/science.1241882.
[14] P.R. Shearing, J. Gelb, N.P. Brandon, X-ray nano computerised tomography of SOFC electrodes using a focused ion beam sample-preparation technique, J. Eur. Ceram. Soc. 30 (2010) 1809–1814, doi:http://dx.doi.org/10.1016/j.jeurceramsoc.2010.02.004.
[15] S. Frisco, A. Kumar, J.F. Whitacre, S. Litster, Understanding Li-Ion Battery Anode Degradation and Pore Morphological Changes through Nano-Resolution X-ray Computed Tomography, J. Electrochem. Soc. 163 (2016) A2636–A2640, doi:http://dx.doi.org/10.1149/2.0681613jes.
[16] M. Stampanoni, A. Groso, A. Isenegger, G. Mikuljan, Q. Chen, A. Bertrand, S. Henein, R. Betemps, U. Frommherz, P. Böhler, D. Meister, M. Lange, R. Abela, Trends in synchrotron-based tomographic imaging: the SLS experience, in: U. Bonse (Ed.), Proc. SPIE, 2006, doi:http://dx.doi.org/10.1117/12.679497 p. 63180M (1–14).
[17] A. Tkachuk, F. Duewer, H. Cui, M. Feser, S. Wang, W. Yun, X-ray computed tomography in Zernike phase contrast mode at 8 keV with 50-nm resolution using Cu rotating anode X-ray source, Zeitschrift Für Krist. – Cryst. Mater. 222 (2007) 650–655, doi:http://dx.doi.org/10.1524/zkri.2007.222.11.650.
[18] C. Rau, U. Wagner, A. Peach, I.K. Robinson, B. Singh, G. Wilkin, C. Jones, R. Garrett, I. Gentle, K. Nugent, S. Wilkins, The Diamond Beamline I13L for Imaging and Coherence, AIP Conf. Proc., American Institute of Physics, 2010, pp. 121–125, doi:http://dx.doi.org/10.1063/1.3463156.
[19] A. Rack, F. Garcia-Moreno, C. Schmitt, O. Betz, A. Cecilia, A. Ershov, T. Rack, J. Banhart, S. Zabler, On the possibilities of hard X-ray imaging with high spatio-temporal resolution using polychromatic synchrotron radiation, J. Xray. Sci. Technol. 18 (2010) 429–441.
[20] E. Maire, P.J. Withers, Quantitative X-ray tomography, Int. Mater. Rev. 59 (2013) 1–43, doi:http://dx.doi.org/10.1179/1743280413Y.0000000023.
[21] F. Tariq, V. Yufit, D.S. Eastwood, Y. Merla, M. Biton, B. Wu, Z. Chen, K. Freedman, G. Offer, E. Peled, P.D. Lee, D. Golodnitsky, N. Brandon, In-Operando X-ray Tomography Study of Lithiation Induced Delamination of Si Based Anodes for Lithium-Ion Batteries, ECS Electrochem. Lett. 3 (2014) A76–A78, doi:http://dx.doi.org/10.1149/2.0081407eel.
[22] J.M. Paz-Garcia, O.O. Taiwo, E. Tudisco, D.P. Finegan, P.R. Shearing, D.J.L. Brett, S. A. Hall, 4D analysis of the microstructural evolution of Si-based electrodes during lithiation: Time-lapse X-ray imaging and digital volume correlation, J. Power Sources. 320 (2016) 196–203, doi:http://dx.doi.org/10.1016/j.jpowsour.2016.04.076.
[23] P. Pietsch, M. Hess, W. Ludwig, J. Eller, V. Wood, Combining operando synchrotron X-ray tomographic microscopy and scanning X-ray diffraction to study lithium ion batteries, Sci. Rep. 6 (2016) 1–10, doi:http://dx.doi.org/10.1038/srep27994 27994.
[24] J. Gonzalez, K. Sun, M. Huang, J. Lambros, S. Dillon, I. Chasiotis, Three dimensional studies of particle failure in silicon based composite electrodes for lithium ion batteries, J. Power Sources. 269 (2014) 334–343, doi:http://dx.doi.org/10.1016/j.jpowsour.2014.07.001.
[25] O.O. Taiwo, D.S. Eastwood, P.D. Lee, J.M. Paz-Garcia, S.A. Hall, D.J.L. Brett, P.R. Shearing, In-Situ Examination of Microstructural Changes within a Lithium-Ion Battery Electrode Using Synchrotron X-ray Microtomography, ECS Trans. 69 (2015) 81–85, doi:http://dx.doi.org/10.1149/06918.0081ecst.
[26] F. Sun, H. Markötter, K. Dong, I. Manke, A. Hilger, N. Kardjilov, J. Banhart, Investigation of failure mechanisms in silicon based half cells during the first cycle by micro X-ray tomography and radiography, J. Power Sources. 321 (2016) 174–184, doi:http://dx.doi.org/10.1016/j.jpowsour.2016.04.126.
[27] O.O. Taiwo, J.M. Paz-García, S.A. Hall, T.M.M. Heenan, D.P. Finegan, R. Mokso, P. Villanueva-Pérez, A. Patera, D.J.L. Brett, P.R. Shearing, Microstructural degradation of silicon electrodes during lithiation observed via operando X-ray tomographic imaging, J. Power Sources. 342 (2017) 904–912, doi:http://dx.doi.org/10.1016/j.jpowsour.2016.12.070.
[28] M.J. Loveridge, M.J. Lain, I.D. Johnson, A. Roberts, S.D. Beattie, R. Dashwood, J.A. Darr, R. Bhagat, Towards High Capacity Li-ion Batteries Based on Silicon-Graphene Composite Anodes and Sub-micron V-doped $LiFePO_4$ Cathodes, Sci. Rep. 6 (2016) 1–11, doi:http://dx.doi.org/10.1038/srep37787 37787.
[29] L.L. Lavery, J. Gelb, A.P. Merkle, A. Steinbach, X-Ray Microscopy for Hierarchical Multi-Scale Materials, Micros. Today. 22 (2014) 16–21, doi:http://dx.doi.org/10.1017/S155192951400056X.
[30] Y. Sagara, A.K. Hara, W. Pavlicek, A.C. Silva, R.G. Paden, Q. Wu, Abdominal CT: Comparison of Low-Dose CT With Adaptive Statistical Iterative Reconstruction and Routine-Dose CT With Filtered Back Projection in 53 Patients, Am. J. Roentgenol. 195 (2010) 713–719, doi:http://dx.doi.org/10.2214/AJR.09.2989.
[31] P. Perona, J. Malik, Scale-space and edge detection using anisotropic diffusion, IEEE Trans. Pattern Anal. Mach. Intell. 12 (1990) 629–639, doi:http://dx.doi.org/10.1109/34.56205.
[32] W.E. Lorensen, H.E. Cline, Marching Cubes: A High Resolution 3D Surface Construction Algorithm, SIGGRAPH Comput. Graph. 21 (1987) 163–169, doi:http://dx.doi.org/10.1145/37402.37422.
[33] R. Fathi, J.C. Burns, D.A. Stevens, H. Ye, C. Hu, G. Jain, E. Scott, C. Schmidt, J.R. Dahn, Ultra High-Precision Studies of Degradation Mechanisms in Aged $LiCoO_2$/Graphite Li-Ion Cells, J. Electrochem. Soc. 161 (2014) A1572–A1579, doi:http://dx.doi.org/10.1149/2.0321410jes.
[34] R. Ruffo, S.S. Hong, C.K. Chan, R.A. Huggins, Y. Cui, Impedance Analysis of Silicon Nanowire Lithium Ion Battery, Anodes J. Phys. Chem. C 113 (26) (2009) 11390–11398.

[35] L. Chen, K. Wang, X. Xie, J. Xie, Effect of vinylene carbonate (VC) as electrolyte additive on electrochemical performance of Si film anode for lithium ion batteries, J. Power Sources. 174 (2007) 538–543, doi:http://dx.doi.org/10.1016/j.jpowsour.2007.06.149.
[36] J. Guo, A. Sun, X. Chen, C. Wang, A. Manivannan, Cyclability study of silicon–carbon composite anodes for lithium-ion batteries using electrochemical impedance spectroscopy, Electrochim. Acta 56 (2011) 3981–3987, doi:http://dx.doi.org/10.1016/j.electacta.2011.02.014.
[37] K. Schroder, J. Alvarado, T.A. Yersak, J. Li, N. Dudney, L.J. Webb, Y.S. Meng, K.J. Stevenson, The Effect of Fluoroethylene Carbonate as an Additive on the Solid Electrolyte Interphase on Silicon Lithium-Ion Electrodes, Chem. Mater. 27 (16) (2015) 5531–5542.
[38] J.P. Schmidt, T. Chrobak, M. Ender, J. Illig, D. Klotz, E. Ivers-Tiffée, Studies on $LiFePO_4$ as cathode material using impedance spectroscopy, J. Power Sources. 196 (2011) 5342–5348, doi:http://dx.doi.org/10.1016/j.jpowsour.2010.09.121.
[39] V. Etacheri, O. Haik, Y. Goffer, G.A. Roberts, I.C. Stefan, R. Fasching, D. Aurbach, Effect of Fluoroethylene Carbonate (FEC) on the Performance and Surface Chemistry of Si-Nanowire Li-Ion Battery Anodes, Langmuir. 28 (2012) 965–976, doi:http://dx.doi.org/10.1021/la203712s.